



# Three-dimensional oxygen concentration monitoring in hydrogels using low-cost phosphorescence lifetime imaging for tissue engineering

XU MEI,<sup>1</sup> QIYIN FANG,<sup>1,2</sup>  AND P. RAVI SELVAGANAPATHY<sup>1,3,\*</sup>

<sup>1</sup>School of Biomedical Engineering, McMaster University, 1280 Main Street W, Hamilton, ON L8S 4L8, Canada

<sup>2</sup>Department of Engineering Physics, McMaster University, 1280 Main Street W, Hamilton, ON L8S 4L8, Canada

<sup>3</sup>Department of Mechanical Engineering, McMaster University, 1280 Main Street W, Hamilton, ON L8S 4L8, Canada

\*selvaga@mcmaster.ca

**Abstract:** Oxygen concentration measurement in 3D hydrogels is vital in 3D cell culture and tissue engineering. However, standard 3D imaging systems capable of measuring oxygen concentration with adequate precision are based on advanced microscopy platforms, which are not accessible in many laboratories due to the system's complexity and the high price. In this work, we present a fast and low-cost phosphorescence lifetime imaging design for measuring the lifetime of oxygen-quenched phosphorescence emission with 0.25  $\mu$ s temporal precision and sub-millimeter spatial resolution in 3D. By combining light-sheet illumination and the frequency-domain lifetime measurement using a commercial rolling-shutter CMOS camera in the structure of a conventional optical microscope, this design is highly customizable to accommodate application-specific research needs while also being low-cost as compared to advanced instruments. As a demonstration, we made a fluidic device with a gas-permeable film to create an artificial oxygen gradient in the hydrogel sample. Dye-embedded beads were distributed in the hydrogel to conduct continuous emission lifetime monitoring when nitrogen was pumped through the fluidic channel and changed oxygen distribution in the sample. The dynamics of the changes in lifetime co-related with their location in the gel of size 0.5 mm $\times$ 1.5 mm $\times$ 700  $\mu$ m demonstrate the ability of this design to measure the oxygen concentration stably and precisely in 3D samples.

© 2023 Optica Publishing Group under the terms of the [Optica Open Access Publishing Agreement](#)

## 1. Introduction

Oxygen concentration is a crucial factor in a variety of biological research settings. Low oxygen tension, or hypoxia, is essential for many normal cellular processes [1], while hypoxia in tumors leads to dysfunctional vascularization and alters cell metabolism [2]. In 3D tissue-engineered constructs, an efficient supply of oxygen by perfusion channels is necessary for the success of tissue growth [3]. Monitoring the oxygen concentration throughout three dimensions in the *in vitro* cell culture constructs/tissue models would be beneficial to understand the underlying cellular mechanisms at the tissue level, as well as to control the product quality in biofabrication to modulate the oxygen supply for optimal cellular growth.

To accommodate the millimeter-size dimensions of typical tissue constructs [4,5], optical imaging methods to measure the oxygen tension are usually favored over Clark electrodes as they are non-invasive, do not consume oxygen in the samples to achieve the sensing, and provide better accuracy and resolution [6,7]. Within these optical methods, quantifying the oxygen's quenching effect on the luminescence emission is a common procedure, where the intensity of

the luminescence is decreased when the excited-state luminophore is deactivated upon contact with the oxygen molecule in the environment. The quenching of luminescence can be described by the Stern-Volmer equation [8]:

$$\frac{I_0}{I} = \frac{\tau_0}{\tau} = 1 + K_{SV}[Q] \quad (1)$$

$I_0$  and  $I$ ,  $\tau_0$  and  $\tau$  are the luminescence intensities and the lifetimes in the absence and presence of the quencher, respectively.  $K_{SV}$  is the Stern-Volmer quenching constant, and  $[Q]$  is the concentration of the quencher, which is the molecular oxygen in this work and referred as the oxygen partial pressure  $pO_2$ .

Change in both intensity and lifetime of the luminescence due to quenching can be used to measure the oxygen concentration. Lifetime measurement is preferred as it is not affected by signal attenuations along various optical paths in the samples. However, luminescence lifetime measurements require considerable expertise and specialized equipment to measure the rapid temporal dynamics of luminescent processes, whose timescales range from nanoseconds to microseconds. Typically, sensitive and high-precision imaging systems like confocal and multiphoton laser scanning microscopes that are very expensive are used and offer gold-standard results, exhibiting capabilities to resolve nanosecond-level fluorescence lifetime and micrometer-scale spatial distribution of oxygen [9–13]. However, the high cost, system complexity, and complicated requirements for the sample preparation hinder their field application in tissue engineering. More recently, several research designs utilizing optical detectors in combination with customized optics have been built for oxygen monitoring in their specific cell culture constructs. Most of them conduct point measurements inside microfluidic chambers or culture mediums by placing the luminescent probes at fixed positions and adjusting the illumination and detector accordingly [14–17]. However, such configurations exhibit low spatial resolution and cannot provide sufficient information to map cellular metabolism with oxygen concentration in 3D. In other studies, 2D/3D oxygen mappings are proposed but still constructed with high-priced and advanced scientific cameras or fluorometers [18–20]. These instruments are designed with a large temporal dynamic range. Nevertheless, since most oxygen-indicating dyes have lifetimes in the range of microseconds, their high capabilities may be redundant and can lead to unnecessary costs. There are also previous studies that have demonstrated the utilization of conventional CCD devices for high temporal resolution measurements. This has been achieved through either low-level hardware control [21,22] or the incorporation of image intensifiers to enable single photon counting [23,24].

A potential cost-effective option for measuring luminescence lifetime based on a consumer-level CMOS camera was proposed previously, leveraging the rolling shutter effect of the camera and conducting frequency-domain lifetime measurement [25]. The rolling shutter CMOS image sensor exposes pixel array to the light signal in a sequential row-by-row manner, as such it is only after the completion of the exposure of every row of pixels that a full image frame is formed. This can allow for less circuitry in each pixel unit, hence larger effective sensing area and higher sensitivity compared to the global shutter, where all the pixels are exposed simultaneously. The rolling shutter mode can lead to image distortion when capturing fast-moving objects. However, its rapid row-scanning speed, exceeding 100 k rows per second, also enables the potential to sample periodic light signals at frequencies much higher than the conventional camera frame rate of 60 fps. This capability makes it possible to measure luminescence lifetimes at the microsecond level by analyzing the fringes shown in the image that arise from the coupling of the image sensor's line-scanning and the intensity-modulated excitation light. In frequency-domain lifetime measurement, the phase delay in the luminescence emission in response to the intensity-modulated excitation is measured to determine the lifetime. The intensity waveforms of both the emission and the excitation signals can be captured and analyzed simultaneously by properly directing them to different regions of the sensor array, all while being scanned by the same pixel row range.

As such the phase shift between the modulated excitation and the corresponding emission can be obtained and translated into the luminescence lifetime. Although innovative, this technique reported a lifetime measurement error out of  $\pm 3 \mu\text{s}$  which corresponds to  $\pm 1.5\%$  of 1 atm  $pO_2$  that may not be suitable for some cell culture applications. Furthermore, due to the use of a film type sensing layer, it was not suited for analysis of 3D oxygen distribution in tissue constructs and hydrogel-based cell culture.

Here we combine the rolling-shutter mode CMOS-camera-based lifetime measurement with polymer microbeads that localize luminescence distributed throughout the 3D hydrogel culture construct when illuminated by a light sheet to determine normoxic to hypoxic oxygen concentration in 3D with a sub-millimeter resolution. We simultaneously developed new data processing methods that enable us to increase the temporal precision to  $\pm 0.25 \mu\text{s}$ , which corresponds to  $\pm 0.2\%$  of 1 atm  $pO_2$ . Finally, we use polymer microbeads to localize and distribute the luminescence dyes over the entire volume of a 3D hydrogel model to determine the oxygen concentration throughout the volume. This design can be easily adapted to customized sample geometries, making it effective in various biological settings. The overall cost of all the system components could be as low as 1500 USD, significantly lower than oxygen imaging solutions using advanced instruments while maintaining competitive performance.

## 2. Materials and methods

### 2.1. Optical system

The optical system is designed to facilitate rapid verification of the proposed low-cost luminescence lifetime determination method integrated on a low power microscope structure equipped with optical sectioning illumination, specifically a light sheet, to conduct 3D examination of the phosphor beads dispersed inside the hydrogel samples. The system comprises two main components: an illumination sub-system (illumination arm) that provides excitation to the phosphorescent probes deployed in the sample and a detection sub-system (detection arm) that collects the emission signals from the probes through the volume of the sample. The configuration of the illumination arm is adapted from an open-source integrated microscopy platform that provides recommendations for selecting user-friendly optical components for constructing a light-sheet setup [26]. The light sheet exhibits inherent optical-sectioning capability, as it illuminates the sample with a planar sheet of light that is comparable in thickness to the depth of field of the detection system [27]. Consequently, this technique can enhance the image contrast by minimizing out-of-focus background noise and reduce phototoxicity to the sample due to the highly confined light exposure.

In the illumination arm, as shown in Fig. 1 with both horizontal and vertical views, the excitation light originates from a laser diode module (Laserland, 405 nm, 200 mW) and is controlled by a driver (12 V/2A DC, 200 mW – 2W) that receives square wave TTL modulation signal (4kHz, 50% duty cycle) from a function generator (Tektronix, AFG 3022B). By adjusting the driving current, the maximum laser output power has been restricted to 100 mW for all the experiments in this work. The output of the laser diode is a diverging elliptical beam circularized by the integrated aspheric lens in the module, resulting in a collimated beam with a 1.5 mm diameter. The light passes through a 3:7 beam splitter (Thorlabs, EBP1) before forming the light sheet. The reflected portion (30%) of the light is coupled to a multimode optical fiber (Corning) and directed to the CMOS sensor as the reference beam. The transmitted portion (70%) forms the light sheet after passing through a 3.5X beam expanding plano-convex lens pair (Thorlabs, LA1131-A  $f = 50$  mm, LA1229-A  $f = 175$  mm), a cylindrical lens (Thorlabs, LJ1695RM-A  $f = 50$  mm), and an objective (Carl Zeiss, 10X 0.22 NA). This straightforward structure offers an approachable light-sheet illumination for performing sub-millimeter optical sectioning on cubic-shaped hydrogel culture constructs. Given that phosphor beads are dispersed within the samples and the optical setup is specifically utilized to examine the phosphorescence

emission from individual probes, the light sheet's characteristics do not need to meet the same stringent requirements as those in 3D structural reconstruction applications.

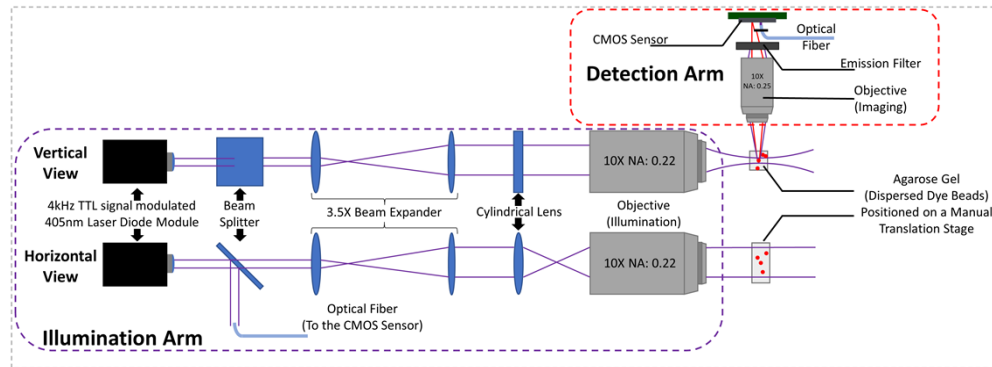


**Fig. 1. Schematic diagram of the optical system.** The low power microscope structure (Detection Arm) incorporates both light-sheet illumination (Illumination Arm) and a rolling shutter CMOS image sensor. Vertical and horizontal views of the illumination arm are provided respectively, showcasing the intersections of the illumination beam with the cubic agarose sample. The cubic sample can be positioned and swept through the illumination plane by utilizing a manual translational stage. To enable simultaneous capture of both excitation and emission signals, a portion of the excitation light is split at the source and directed to the CMOS sensor in the detection arm via optical fibers. This configuration allows the CMOS sensor to record both the excitation light and the phosphorescence emission concurrently.

The detection arm shown in Fig. 1 is positioned orthogonally to the plane of the light sheet. An imaging objective (Olympus, 10X Plan C Achromatic Dry Objective, infinity-corrected, 0.25 NA) collects the phosphorescence emission from the phosphor probes excited by the light-sheet illumination in the agarose gel sample. After passing through an emission filter (Semrock, FF01-593, 593 nm long-pass), images of the phosphorescence light form on the CMOS sensor, while approximately 25% of the sensor area is reserved for recording the excitation light spots by attaching a 3d-printed socket that holds the output end of the optical fibers towards the sensor. The interference between the excitation and emission signals is avoided since the fiber socket shields the sensor area where the excitation spots lie. Therefore, light spots from the excitation signal directed by the optical fibers and the phosphorescence emission from the phosphor probe can be captured by the CMOS sensor at the same time. This simultaneous capture of two signals enables the frequency-domain luminescence lifetime measurement leveraging the rolling shutter scanning effect, which will be discussed in the following subsections. The positions of both the sample and the imaging arm can be tuned using manual translational stages, enabling adjustments of the illumination plane and the focal plane of the imaging objective for examining different depths of the hydrogel sample.

The infinity-corrected objective adopted in the detection arm is designed to ensure that all light rays originating from a single point on the specimen, at the objective's working distance, exit the objective in a parallel way. In the standardized configuration, this objective requires the coupling with a tube lens to converge the light rays and form an image [28]. However, the cost of a tube lens could be comparable to the total cost of the other components. Alternatively, the infinity-corrected objective can still produce images without a tube lens by adjusting the specimen's position further away from the focal plane (working distance), following the lens equation. This adjustment introduces enhanced spherical aberration, which we find tolerable as our focus is not on capturing the structural details of the sample. Instead, we are examining the

rolling shutter scanning fringes across considerably large areas on the sensor. As a result, the detection arm features a simplified microscope structure.

## 2.2. Phosphorescence lifetime measurement using the rolling shutter CMOS sensor

Determination of phosphorescence lifetimes from probes throughout the culture construct's volume is the key process of 3D oxygen monitoring in this work. We utilized a phosphorescence dye (PtTFPP) that has a lifetime ranging from 21  $\mu\text{s}$  to 70  $\mu\text{s}$  [29], corresponding to air-equilibrated (20.9% of 1 atm  $pO_2$ ) and oxygen-depleted (0% of 1 atm  $pO_2$ ) conditions, respectively. Even though the phosphorescence lifetime of this dye is in microsecond range, measurement of the exponential decay in phosphorescence intensity (time-domain) requires high sensitivity and megahertz-level sampling rate to resolve the decaying curve, which can only be achieved with expensive devices like silicon photomultiplier or avalanche photodiode rather than a commercial image sensor [30]. An alternative way is to utilize the rapid lifetime determination (RLD) algorithm which only requires a limited number of images to determine the parameters of a single decaying process but needs low-level hardware control to ensure high synchronization between the image sensor capturing and the excitation signal [31].

The cost-effective lifetime measuring approach proposed in this work leverages the use of the rolling-shutter effect in consumer-level CMOS cameras to perform high-fidelity frequency-domain lifetime measurement through data processing. Unlike the time-domain method, which uses a single short pulse for excitation, the frequency-domain method utilizes continuous but sinusoidally modulated excitation. This results in the continuous emission from the phosphors which follows the modulation frequency of the excitation while exhibiting a phase difference due to the decaying nature of the excited states of the phosphor molecules. Consequently, the phase shift between the intensity waveforms of the emission and the excitation is related to the exponential decay lifetime characteristic in single pulse excitation. The relationship between the lifetime and the phase shift can be described in the equation below [8]:

$$2\pi f_{\text{mod}} \tau_{\text{lifetime}} = \tan \varphi_{\text{phase shift}} \quad (2)$$

To restore the phase shift, the rolling shutter effect is leveraged as a fast-sampling mechanism. Pixels on the rolling shutter mode CMOS sensor are sequentially activated in rows rather than all at once, as in global shutter mode. Since the temporal behaviors of all the pixels in the same row are consistent, the position of the image of the phosphor probe is tuned to cover the same range of pixel rows as the excitation light spot, as shown in Fig. 2(a). As such, the excitation and the emission signals can be recorded simultaneously through the pixel integration processes, maintaining their phase difference. When both the excitation and emission signals vary periodically at the same frequency, this results in fringe patterns as shown in Fig. 2(b), due to different rows of pixels integrating the signal at different times and leading to variations in brightness across the captured image and the light spot. As depicted in Fig. 2(c), the least square curve regression algorithm was applied to the readout sequences of the fringe patterns to extract the phase shift between the excitation and the emission signals. At least 3 modulation cycles were included in the regions of interest (ROIs) for accurate phase extraction, corresponding to 100-120 rows in ROI heights. The readouts on the same row were summed up to increase the signal-to-noise ratio, corresponding to 90-200 pixels in ROI widths which also depended on the light spot sizes. The lifetime of the phosphorescence emission can be calculated using Eq. (2) once the phase shift is obtained.

To achieve a suitable dynamic range of the phase shift in response to changes in oxygen concentration, the modulation frequency was chosen at 4kHz to accommodate the range of lifetime changes of the dye (PtTFPP) that would be typically encountered in cell culture applications. This range phase shift range is 0.505-1.053 rad which corresponds to the dye's lifetime range



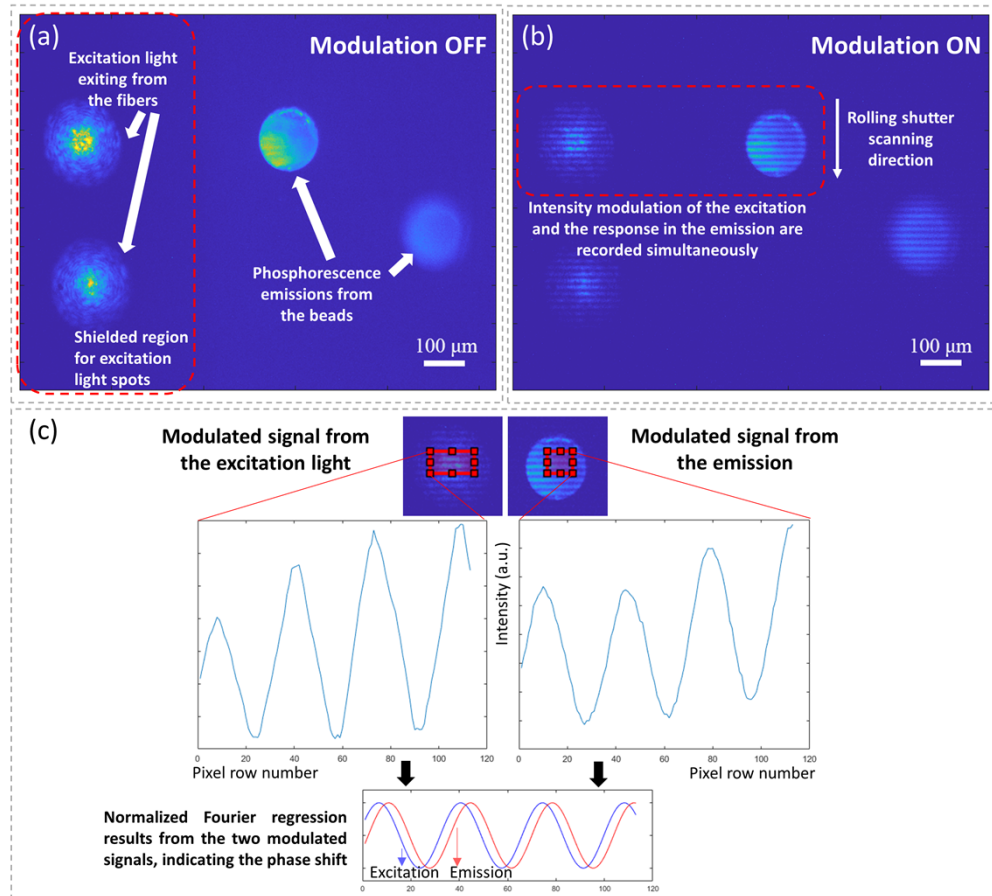


**Fig. 2. Determination of the phase shift of the phosphorescence emission from the modulated excitation.** (a) False color image with light spots exiting from the optical fibers and the emissions from the PS beads. Modulation in the illumination was disabled. (b) False color image of the 4kHz transistor-transistor logic (TTL) modulated excitation light spot and the corresponding emission from the PS beads. The position of the in-focus bead image was tuned to lie on the same span of rows with respect to the reference light spot on the left. (c) The readouts are plotted along the row number, and the phase shift between the excitation and emission signals is calculated by the curve regression using the first-order Fourier series.

from 22  $\mu\text{s}$  to 70  $\mu\text{s}$ , according to Eq. (2). In this work, the temporal activation offset between the consecutive rows in the camera (Alvium 1800U 501 m NIR, image sensor: ON Semi AR0522) is approximately 7  $\mu\text{s}$ . This means the integration window of each row of pixels is delayed for 7  $\mu\text{s}$  with respect to the integration window of the previous row. As a result, pixel readout values along the rows can be regarded as a temporal sampling sequence at the rate of the rolling shutter scanning speed, i.e., around 140 kHz. The use of frequency domain analysis instead of time domain reduces the requirement of speed for data acquisition and the 140 kHz scanning rate of the rolling shutter can effectively capture the phase shifts between two 4 kHz sinusoidal-shaped light signals. We chose a 146  $\mu\text{s}$  pixel exposure time to conduct low-pass integration filtering on the high-frequency components in the square wave-modulated signals since the low-cost laser diode illumination system can only accept transistor-transistor logic (TTL) control.

### 2.3. Phosphor-embedded microbead preparation

Spherical-shaped phosphor-embedded luminescent polymer beads were designed so that they can be conveniently integrated into customized cell culture constructs throughout its volume to enable spatial mapping of the oxygen concentration. As shown in Fig. 3(a), 130 $\mu\text{m}$ -diameter phosphor-embedded (platinum(II)-5,10,15,20-tetrakis-(2,3,4,5,6-pentafluorophenyl)-porphyrin, PtTFPP, Frontier Scientific) polystyrene (PS, Sigma-Aldrich, average  $M_w \sim 280,000$  by GPC) beads are utilized in this work. They were fabricated using a co-flow glass capillary fluidic device [32]. Precise control of the particle diameter can be achieved by setting different injection rates of the polymer solutions during the fabrication process, as the extent of luminescence quenching is subject to the variation of the quencher's diffusion process in the dye-supporting polymer matrix [33]. Beads with diameters in 130 $\mu\text{m}$  were fabricated by setting a 10 mL/h injection rate of 5%wt polyvinyl alcohol (Sigma-Aldrich,  $M_w$  13,000-23,000, 87-89% hydrolyzed) in water and a 2 mL/h injection rate of 1%wt 600:1 polystyrene/dye mixture in dichloromethane (Sigma-Aldrich, anhydrous,  $\geq 99.8\%$ ), where the glass capillaries with 1.3 mm/0.5 mm inner diameters were utilized. The uniform-size beads allow the embedded phosphors to exhibit a consistent response to the oxygen concentration changes in terms of the luminescence lifetime, excelling other geometries of probes.

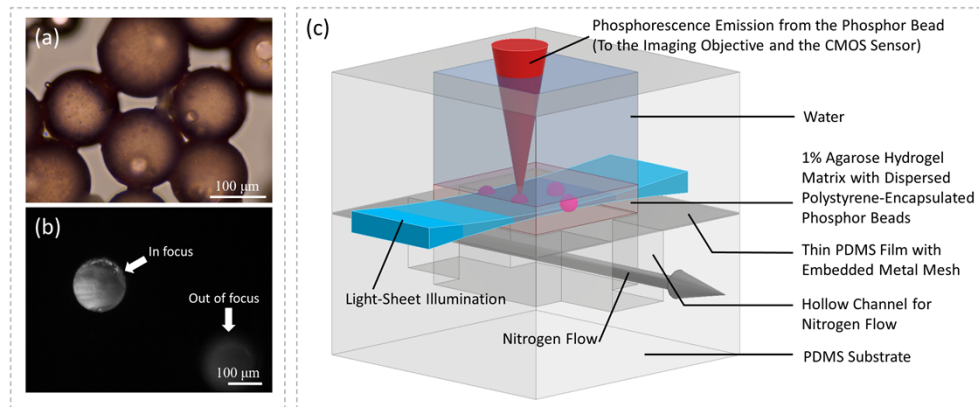


**Fig. 3. Experiment setups.** (a) 40X microscopic image of dye-embedded (PtTFPP) polystyrene (PS) beads. (b) Image of the phosphorescence emissions from the PS beads captured by the optical setup shown in Fig. 1. (c) The 3D model of the PDMS fluidic device for creating oxygen gradients in hydrogel samples. The directions of the light-sheet illumination and the signal detection are presented.

Figure 3(b) depicts the excited polymer beads dispersed within agarose gel, as observed through the proposed optical setup. While the image of the illuminated bead in the foreground is sharp, scattered light from this bead can illuminate neighboring beads that are situated out of the focal plane. Nonetheless, the signal from the in-plane bead remains clear and focused, exhibiting minimal background noise. Adjusting the bead density within the gel to ensure adequate separation can prevent interference of the emission signals during imaging, while still maintaining sufficient spatial resolution for accurate measurements in hydrogel samples.

#### 2.4. Microfluidic hydrogel platform

To assess the system's spatial resolution and temporal precision in the context of 3D live cell constructs, a fluidic device that can generate varying millimeter-scale artificial oxygen gradients in agarose hydrogel samples was developed. Figure 3(c) shows the 3D model of this device. A 1 cm<sup>3</sup> well is built above a metal-mesh-embedded thin gas-permeable PDMS film, which supports the well over a hollow channel for nitrogen flow. A 2mm-thick layer of agarose gel, mimicking the cell culture environment, contains randomly distributed phosphor-embedded beads and is placed at the bottom of the well. Water is added to the well, up to the opening that will be later sealed by a cover glass to eliminate the image distortion caused by the surface curvature at the water-air interface. When nitrogen is pumped through the channel beneath the well, oxygen will be depleted in the gel layer in the vicinity of the channel setting up a millimeter-scale oxygen gradient ranging from oxygen-depleted to air-equilibrated levels within the agarose gel sample.

As shown in Fig. 3(c), the light sheet can illuminate and excite the phosphor beads in a horizontal layer of the agarose gel, with the upward portion of the emission collected by the detection arm. By synchronously adjusting the position of the cubic sample and the focal plane of the imaging objective using a pair of manual translational stages, the emission from the probes at different depths can be examined. This enables the measurement of oxygen concentration at arbitrary locations within the hydrogel sample if the phosphor bead is properly positioned.

#### 2.5. Image acquisition and data processing software

The Alvium 1800U 501 m NIR camera (Allied Vision) in the optical setup for image acquisition is driven by the Python script that utilizes Vimba SDK (software suite for machine vision and CSI-2 cameras, Allied Vision). To achieve an optimized frame rate (60 Hz) and the fastest rolling shutter scanning speed (7  $\mu$ s/row), the camera is set in free-run mode, continuously streaming raw pixel data into the buffer during the experiment. The acquisition process involves capturing the data from the buffer and writing it to the hard drive as image files through the script. The script is designed to synchronize the light-sheet illumination with the acquisition process, allowing control over the illumination period and the number of consecutive frames being generated for each capture.

The data analysis is performed using MATLAB (Mathworks) programs. A GUI program based on MATLAB App Designer (Mathworks) has been developed to enable manual selection of regions of interest (ROIs) in the acquired images and display the corresponding fringes. Additionally, a separate script has been written to implement least-square sinusoidal curve regression over the ROIs and extract the phase shift between the excitation and emission signals. The curve regression script also allows for assigning the number of consecutive frames to conduct averaging of the phase shift over the selected ROIs.



### 3. Results and discussion

#### 3.1. Precise phosphorescence lifetime determination from spherical polymer beads dispersed in the hydrogel model

Owing to light scattering and attenuation in the sample and the characteristics of the optical fiber, the brightness within the regions of interest (ROIs) is non-uniform and is related to the sample's physical geometry, as Fig. 4(a) shows. This non-uniformity can affect the accuracy of the phase extraction process, which relies on all the readouts within a region to resolve the intrinsic modulated sinusoids. When the signal amplitude at each pixel varies, the weight of each data point will differ during the regression process, resulting in deviations of the calculated phase shift from the true value between the excitation and emission sinusoids. As shown in Fig. 4(b), since the phases of the intrinsic sinusoids proceed a certain step when the new frame is captured by the camera, the distortions on the sinusoidal signals are different in the two consecutive frames, leading to varied curve regression results. Those image brightness “envelopes”, which are due to the complicated light scattering along the optical paths and various geometries of the samples, are difficult to predict apriori and can potentially limit the use of lifetime measurement utilizing the rolling shutter effect in real applications, where the sample geometries can vary and be restricted by other technical considerations.

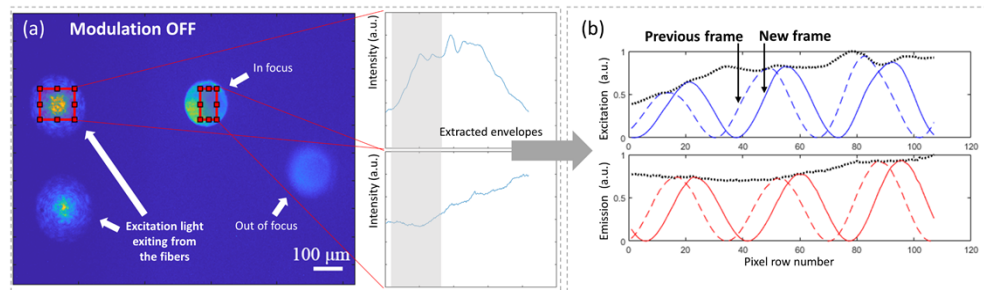


**Fig. 4. Demonstration of envelope-affected signal detection.** (a) Non-uniformity in the image brightness in normal constant illumination. “Envelope” patterns from the two regions of interest (excitation and emission, respectively) are extracted and plotted along the row number. (b) Difference in the distortion of the modulated signals between the consecutive frames due to the non-uniformity in the image brightness (envelopes extracted from the gray areas). Since the consecutive frames are captured at different time points, the intrinsic modulation will undergo a phase increment, resulting in differently distorted fringe patterns extracted from the two frames over the same ROIs.

Figure 5(a) shows the phase shift values extracted from 800 successive frames captured at 68.125 fps from a polymer bead (probe) placed in an environment where the oxygen concentration was gradually decreasing. While the overall trend of increasing phase shift can be observed, the wide dispersion of the data points made it difficult to resolve minor variations in the phase shift accurately.

However, further data analysis can solve this issue. As illustrated in Fig. 5(b), given that the intrinsic modulated signal underwent approximately  $2\pi$  for every 8 frames when the camera was freely running at 68.125 fps, with only a slight variation relative to the initial phase recorded 7 frames earlier, we can collect every 8<sup>th</sup> frame into a separate group. This yielded 7 groups of sinusoid-like sequences out of the scattered point set. The continuous pattern was foreseeable since each rearranged sequence was equivalent to the outcome of a virtual image-capturing process where the phase changes of the intrinsic signals between successive frames were minimal, unlike the large increments shown in Fig. 4(b). The patterns indicate that there were underlying mechanisms in the distributions of the signal as shown in Fig. 5(a).

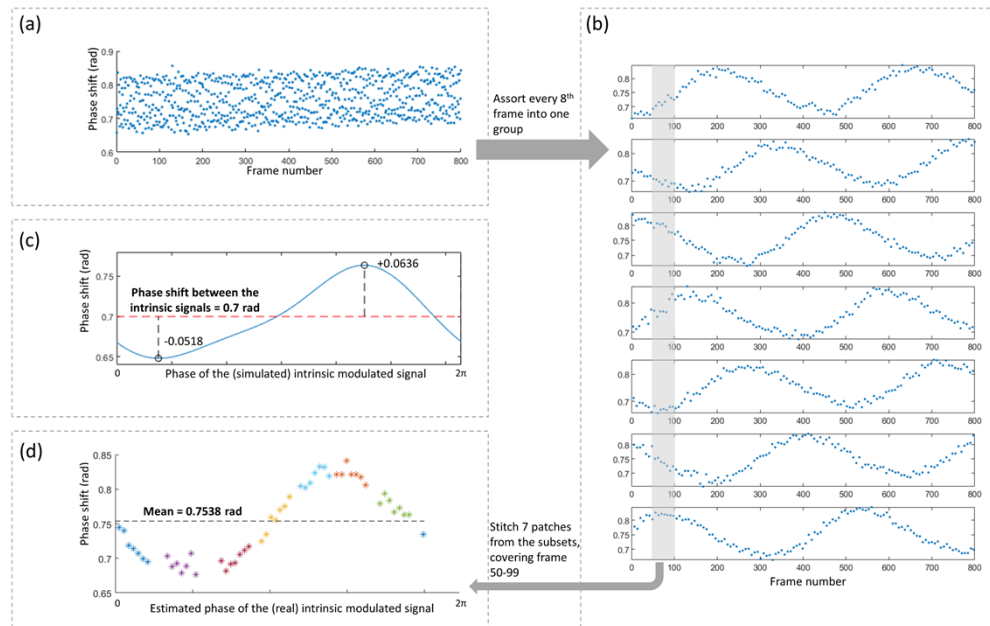


**Fig. 5.** Procedures of data analysis for phase shift determination based on the scattered measurement results. (a) Phosphorescence emission phase shift values from a fixed probe extracted from 800 successive frames captured at 68.125 fps. The values are plotted against the frame number, showing an ascending trend while the oxygen level around the probe is decreasing. (b) 800 data points in (a) are assorted by putting every 8<sup>th</sup> frame into one group while maintaining the original order. Each of the groups exhibits a similar sinusoid-like pattern. (c) Simulated phase shift extraction results by applying least square regression on the real brightness envelope-modified ideal sinusoid pair with a preset phase difference (0.7 rad as a demonstration). (d) Rearranged 50 successive data points according to their relative positions on the sinusoid-like phase shift-phase of modulation curve estimated from the patterns of 7 rearranged point groups.

To evaluate the scattering patterns of the calculated phase shift values, we conducted a fringe pattern simulation that combined the envelopes extracted from Fig. 4 with a pair of ideal sinusoids with preset phase difference which mimicked the modulated excitation and the corresponding phosphorescence emission. In Fig. 5(c), the simulated phase shifts calculated using the previous regression method are plotted against the initial phases of the intrinsic sinusoids from 0 to  $2\pi$ , with the preset phase shift at 0.7 rad. It is evident that the curve is sinusoid-like regardless of changes in the envelopes, but the troughs and the crests are usually not symmetric. However, the integral mean of this curve aligns well with the preset phase shift value, which also holds for other values besides 0.7 rad. This suggests an averaging strategy can be applied to stabilize the measurement of emission phase shift.

Picking 50 successive data points (frame 50-99) from Fig. 5(a), we estimated the relative phase of each point's corresponding intrinsic signals according to the rearranged subsets and replotted these 50 points over a  $2\pi$  span based on the estimation, as shown in Fig. 5(d). It is akin to stitching 7 data point patches (each patch was assigned a unique color in the figure) from each of the subsets. The resulting data distribution has a sinusoid-like shape consistent with the curve we obtained from the simulation, with an average of 0.7538 rad, corresponding to the lifetime at 37.35  $\mu$ s. As the extracted phase shift values from the 50-frame cluster can uniformly sample the curve shown in Fig. 5(c) over the whole span, it proved that an averaging strategy of taking 50

frames for a phase shift measurement can closely estimate the true intrinsic phase shift value and eliminate the “envelope” effect caused by the brightness non-uniformity in the captured image.

When a CMOS camera with a different rolling shutter scanning speed and frame rate is used, the frame cluster size for the averaging process can be determined by the coupling between the free-running image capture and the signal modulation. A similar rearrangement of the scattered data point set into several subsets with continuous patterns, as in Fig. 5(b), should be obtained through experiments. The minimal number of frames to conduct the average strategy is equivalent to the amount needed to reconstruct the sinusoid-like curve, as Fig. 5(d) shows.

### 3.2. Assessing the consistency of the lifetime measurement with constant environmental conditions

The brightness non-uniformity in the image makes the phase shift values extracted from the individual frames differ from each other. By utilizing the average strategy proposed in the previous section, this lifetime measurement technique can closely approximate the true value distorted by the brightness “envelope”. However, the “envelope” itself has temporal variations at a larger timescale compared to the capture process of a frame cluster, i.e., the brightness distribution within the ROI can change during the long experiment procedure even in the absence of external interference. In practical scenarios, these changes may be attributed to fluctuations in illumination intensity or slight displacements of the probes within the soft cell culture matrix. To assess the long-duration lifetime measurement stability of this design and guarantee its reproducibility for the same measured quantity, we conducted an experiment of continuous phosphorescence lifetime monitoring on a single bead within an air-equilibrated 1% agarose hydrogel matrix over 1500 seconds. The 1% agarose in water solution was heated in a 1500W microwave oven for 25 seconds, poured into a plastic cuvette, mixed with dye-embedded PS beads, and cured for 15 minutes while fully exposed to air. The sample was installed onto the imaging system in this work and one bead within the matrix was selected for continuous monitoring. For every 5 seconds, a cluster of 50 consecutive frames was captured at 68.125 fps. While the camera was on standby, the illumination was turned off by a relay to prevent thermally induced lifetime changes.

Figure 6(a) explicitly shows the brightness “envelope” changes in the phosphorescence emission during the experiment without any external disturbance. The amplitudes of the recorded signals exhibited an increasing trend from 500 s to 1500 s. All 15000 lifetime measurements from 300 50-frame clusters were plotted in Fig. 6(b) along with the standard deviations of the lifetime values (right y-axis) within each frame cluster, indicating the width of the lifetime distribution of each cluster which relates to the “envelope” changes. It turned out that slight differences in the signal amplitudes can lead to large variations in the extracted phase shift values from individual frames.

Figure 6(b) shows the corresponding averaged data points obtained from every cluster of 50 successive frames. Figure 6(d) presents the distribution histogram of the 300 averaged data points, with over 90% of the measurement results lying within a  $0.2 \mu\text{s}$  span. The experiment shows that profiling the continuously changing and highly arbitrary envelope is impractical and unnecessary. By applying the averaging strategy, we achieved a  $\pm 0.25 \mu\text{s}$  lifetime measurement error range, which corresponds to a  $\pm 0.2\%$  of 1 atm  $pO_2$  accuracy for monitoring oxygen concentration, over the entire 1500-second experiment under unchanged conditions with unpredictably changing image brightness. This analysis suggests the high-resolution measurement of the phosphorescence lifetime, and hence the oxygen concentration can be ensured over long durations of time in applications such as tissue engineering which require the culture of cells from hours to several days, over which the illumination conditions can change.

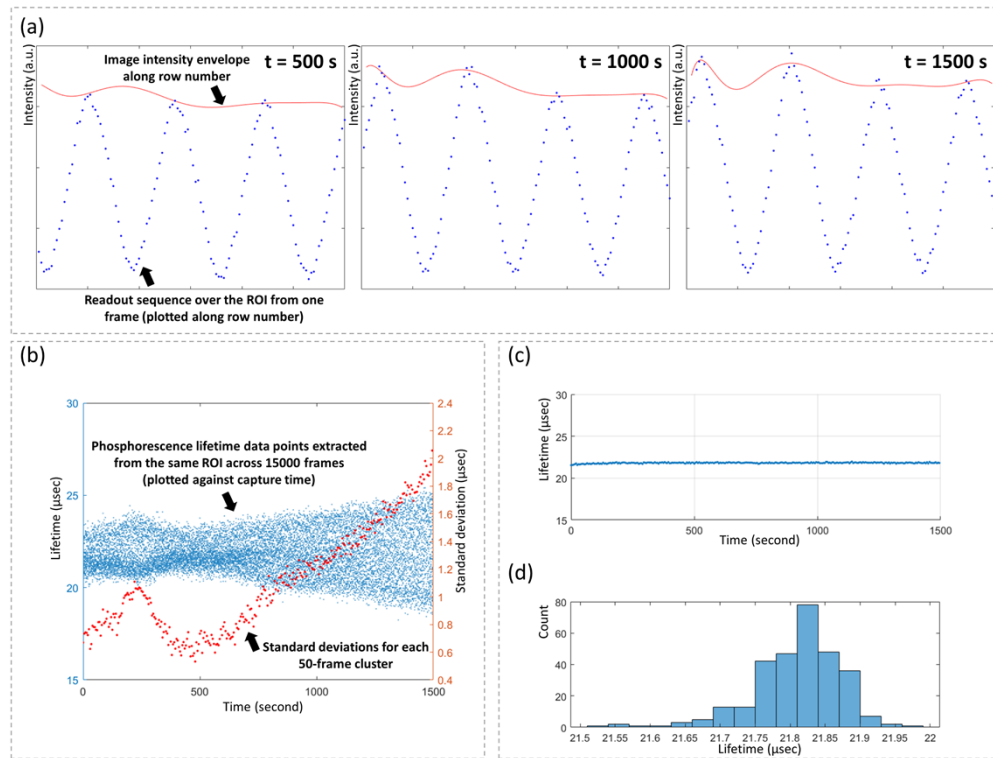


**Fig. 6.** (a) Pixel readout sequences over the same ROI (emission) at 500 s, 1000 s, and 1500 s. In each subfigure, data points were extracted from one single frame, with the envelope obtained from the neighboring 100 frames. (b) Phosphorescence lifetime monitoring results from a probe placed in agarose gel in a constant air-equilibrated condition for 1500 seconds. 50 successive frames were captured every 5 seconds. The standard deviations of the lifetime values within each cluster are plotted with respect to the right y-axis, indicating a gradual and continuous brightness envelope change in the captured image sequence. (c) Averaged lifetime values throughout the experiment duration according to the proposed averaging strategy. (d) Histogram of 300 lifetime values from the averaging results. 90% of the points lie in a 0.2  $\mu\text{s}$  span, where the overall distribution is within 0.5  $\mu\text{s}$ .

Additionally, by applying Eq. (1) and (2), we establish a relationship between the measured phase shift and the corresponding oxygen partial pressure:

$$pO_2 = \frac{1}{K_{SV}} \left( \frac{2\pi f_{mod} \tau_0}{\tan \varphi_{phase\ shift}} - 1 \right) \quad (3)$$

To measure oxygen partial pressure below normoxic conditions, current accuracy in the phase shift measurement based on the rolling shutter scanning technique provides reduced error in environments with lower oxygen levels due to the inverse relationship between the two quantities. This theoretical evidence validates the efficacy of the design for tissue/cell culture applications, where passive oxygen diffusion from air maintains oxygen levels ranging from 18% to below 5% due to various cellular oxygen-consuming activities.

### 3.3. Resolving artificial oxygen gradient in the 3D cell culture model

The primary objective of this design is to resolve phosphorescence lifetime in 3D for oxygen concentration mapping throughout the volume of tissue engineering samples. To evaluate the system performance of resolving small-scale oxygen gradient in 3D cell culture constructs, we deployed phosphorescent probes inside the agarose hydrogel matrix to mimic the examination of cell culture construct using this system. The dye-embedded PS beads were distributed inside an agarose gel layer that was fabricated by the same procedure in the previous section and placed on top of a PDMS fluidic channel as shown in Fig. 3(c). The spatial positions above the channel of four of these beads were measured using a microscope and are shown in Fig. 7(a).

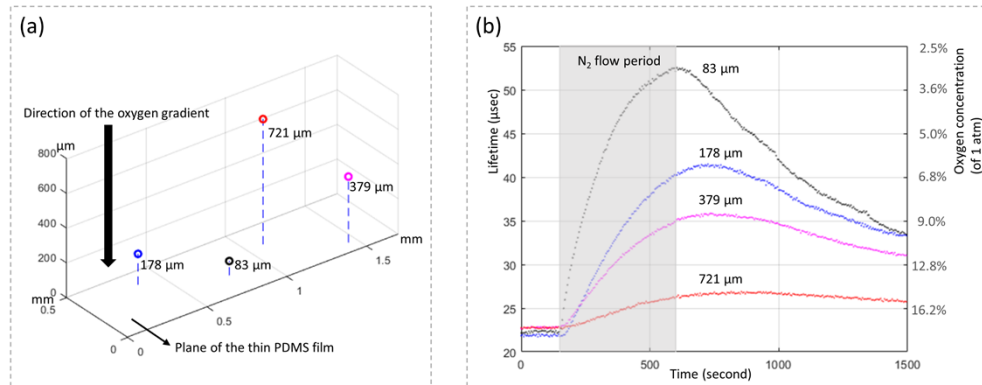


**Fig. 7.** (a) Relative positions of 4 phosphor beads within the agarose gel in an artificial downward oxygen gradient. Beneath the thin film is the nitrogen flow. Above the film is the agarose gel with dispersed phosphor beads. (b) 1500 seconds of lifetime monitoring of the emission from the 4 chosen phosphor beads at different heights above the thin gas-permeable film in the agarose gel sample. Nitrogen flow started at 150 seconds and ceased at 600 seconds. Oxygen concentration values corresponding to the lifetime values on the ticks are labeled on the right y-axis. Note that the concentration values are non-linear with respect to the axis ticks. Bead positions and the corresponding curves are drawn in different colors for distinction.

Since the phosphorescence examination is conducted by tuning the manual translational stages, four separate imaging trials with 1500 seconds duration were conducted on each bead, with 1.5 hours for re-equilibration in between. The image capture and illumination were synchronized as described in section 3.2, with 50 consecutive frames captured every 5 second. Nitrogen was pumped through the hollow channel underneath the gel layer in the period indicated in Fig. 7(b) (150 s-600 s with respect to the start point), which diffuses nitrogen into the region in the gel in



its vicinity and creates an oxygen gradient by passive oxygen diffusion through the gel layer. The continuous phosphorescence lifetime measurements performed on four of these beads are shown in Fig. 7(b) and follow the change in oxygen concentration with time at these locations. The changes in the lifetime are negatively correlated to their distance from the channel as expected indicating that this method can be used to measure dynamic changes in oxygen concentration inside the bulk of hydrogels. According to the linearity between the lifetime and the partial pressure described in Eq. 1, the Stern-Volmer constant can be estimated by two endpoints of the lifetime-oxygen partial pressure curve ( $21\ \mu\text{s} - 21\% pO_2$ ,  $70\ \mu\text{s} - 0\% pO_2$ ) provided in [29]. As such, the right y-axis in Fig. 7(b) shows the approximated oxygen partial pressure in percentages of 1 atm responding to the ticks on the left lifetime axis. Since these phosphorescence probes were positioned within a span of  $0.5\text{mm} \times 1.5\text{mm} \times 700\mu\text{m}$ , it suggests that this design can achieve sub-millimeter spatial resolution, making it compatible with the requirements for oxygen concentration monitoring of a broad range of tissue engineering research. It also indicates a high dynamic range ( $45\ \mu\text{s}$ - $70\ \mu\text{s}$ ) when measuring low oxygen levels (below 5% of 1 atm) based on phosphorescence lifetime, providing excellent resolution in terms of the oxygen concentration and the potential of implementation in hypoxia-related culture experiments as described by Eq. (3).

Although each curve is internally consistent with an error range of  $\pm 0.25\ \mu\text{s}$ , their initial lifetime under the same conditions can differ by up to  $1\ \mu\text{s}$  from one another, which can be observed in Fig. 7(b). This variation is attributable to differences in particle sizes, which result in distinct gas diffusion rates and the consequent varying degrees of phosphorescence quenching inside the beads. To address this issue, potential improvements could involve using smaller diameter beads and implementing more precise particle synthesis techniques.

Since 3D cultures are increasingly used as tissue surrogates, it is crucial to assess whether 3D culture protocols can provide an adequate oxygen level for studying physiopathological processes [34]. Many culture designs rely on millimeter-sized cubic hydrogel constructs, where oxygen is passively diffused from the atmosphere. Oxygen permeability has been engineered [35] or extensively examined in the hydrogel matrix [20,36] for improved manipulation of tissue samples. However, these attempts have proven to be still costly [37,38] or have resulted in insufficient 3D information [39]. In this regard, our system evaluation experiment, which incorporates an artificial oxygen gradient, demonstrates significant potential for implementing a cost-effective and viable 3D oxygen level measurement design in such applications. For future investigations on oxygen distribution or pericellular oxygen tension monitoring in real cell culture scenarios, it is necessary to explore specific methods and patterns for deploying phosphor beads in conjunction with the construct designs. For instance, employing a 3D probe array with equally spaced individual beads would be more advantageous than the random bead distribution proposed in this section, as it would enable a more rigorous mapping of oxygen levels in the 3D environment.

#### 4. Conclusion

Oxygen concentration is a crucial factor in cell viability and metabolic activities for both *in vivo* and cell culture environments. Therefore, monitoring oxygen levels is a vital aspect of tissue engineering research. However, accurate measurement of oxygen concentrations in 3D typically requires expensive and complex instrumentation to quantify phosphorescence lifetime, which can be a barrier for research groups with a biological or clinical background. To address this issue, we have proposed, implemented, and evaluated a low-cost design for conducting 3D phosphorescence lifetime imaging inside hydrogel samples to accurately measure oxygen concentrations. Our proposed design is competitive with existing solutions that use either integrated advanced imaging systems or customized single-point detection, but it comes at a significantly lower cost while maintaining satisfactory performance. With a temporal precision of  $\pm 0.25\ \mu\text{s}$ , our design can resolve sub-millimeter oxygen gradients, achieve a  $\pm 0.2\%$  of 1 atm  $pO_2$  accuracy for monitoring oxygen concentration, and be adaptable to a broad range of sample geometries. This makes it a

suitable option for peer researchers to quickly implement 3D oxygen concentration monitoring with dramatically reduced barriers to entry.

**Funding.** Natural Sciences and Engineering Research Council of Canada; Canadian Institutes of Health Research.

**Disclosures.** The authors declare no conflicts of interest.

**Data availability.** The data underlying the results presented in this paper are not publicly available at this time but may be obtained from the authors upon reasonable request.

## References

1. S. M. Grist, K. L. Bennewith, and K. C. Cheung, "Oxygen Measurement in Microdevices," *Annu Rev. Anal. Chem.* **15**(1), 221–246 (2022).
2. B. Muz, P. de la Puente, F. Azab, and A. K. Azab, "The role of hypoxia in cancer progression, angiogenesis, metastasis, and resistance to therapy," *Hypoxia* **3**, 83–92 (2015).
3. R. L. Wilson, J. P. Connell, and K. J. Grande-Allen, "Monitoring Oxygen Levels within Large, Tissue-Engineered Constructs Using Porphyrin-Hydrogel Microparticles," *ACS Biomater. Sci. Eng.* **5**(9), 4522–4530 (2019).
4. A. Shahin-Shamsabadi and P. R. Selvanapathy, "A rapid biofabrication technique for self-assembled collagen-based multicellular and heterogeneous 3D tissue constructs," *Acta Biomater.* **92**, 172–183 (2019).
5. A. Shahin-Shamsabadi and P. R. Selvanapathy, "Tissue-in-a-Tube: three-dimensional in vitro tissue constructs with integrated multimodal environmental stimulation," *Mater Today Bio* **7**, 100070 (2020).
6. S. M. Grist, L. Chrostowski, and K. C. Cheung, "Optical oxygen sensors for applications in microfluidic cell culture," *Sensors* **10**(10), 9286–9316 (2010).
7. O. S. Wolfbeis, "Luminescent sensing and imaging of oxygen: fierce competition to the Clark electrode," *BioEssays* **37**(8), 921–928 (2015).
8. J. R. Lakowicz, *Principles of fluorescence spectroscopy* (Springer, 2006).
9. J. A. Spencer, F. Ferraro, E. Roussakis, A. Klein, J. Wu, J. M. Runnels, W. Zaher, L. J. Mortensen, C. Alt, R. Turcotte, R. Yusuf, D. Cote, S. A. Vinogradov, D. T. Scadden, and C. P. Lin, "Direct measurement of local oxygen concentration in the bone marrow of live animals," *Nature* **508**(7495), 269–273 (2014).
10. M. F. Wesseler, M. N. Johansen, A. Kiziltay, K. I. Mortensen, and N. B. Larsen, "Optical 4D oxygen mapping of microperfused tissue models with tunable *in vivo*-like 3D oxygen microenvironments," *Lab Chip* **22**(21), 4167–4179 (2022).
11. H. Kurokawa, H. Ito, M. Inoue, K. Tabata, Y. Sato, K. Yamagata, S. Kizaka-Kondoh, T. Kadonosono, S. Yano, M. Inoue, and T. Kamachi, "High resolution imaging of intracellular oxygen concentration by phosphorescence lifetime," *Sci. Rep.* **5**(1), 10657 (2015).
12. S. Kalinina, J. Breymayer, K. Reef, L. Lilge, A. Mandel, and A. Rück, "Correlation of intracellular oxygen and cell metabolism by simultaneous PLIM of phosphorescent TLD1433 and FLIM of NAD(P)H," *J. Biophotonics* **11**(10), e201800085 (2018).
13. H. Choi, D. S. Tzeranis, J. W. Cha, P. Clémenceau, S. J. G. de Jong, L. K. van Geest, J. H. Moon, I. V. Yannas, and P. T. C. So, "3D-resolved fluorescence and phosphorescence lifetime imaging using temporal focusing wide-field two-photon excitation," *Opt. Express* **20**(24), 26219–26235 (2012).
14. E. J. Mahoney, H.-H. L. Hsu, F. Du, B. Xiong, P. R. Selvanapathy, and Q. Fang, "Optofluidic Dissolved Oxygen Sensing With Sensitivity Enhancement Through Multiple Reflections," *IEEE Sens. J.* **19**(22), 10452–10460 (2019).
15. B. Xiong, E. Mahoney, J. F. Lo, and Q. Fang, "A Frequency-domain optofluidic dissolved oxygen sensor with total internal reflection design for in situ monitoring," *IEEE J. Sel. Top. Quantum Electron.* **27**(4), 6900107 (2020).
16. F. Wang, L. Chen, J. Zhu, X. Hu, and Y. Yang, "A Phosphorescence Quenching-Based Intelligent Dissolved Oxygen Sensor on an Optofluidic Platform," *Micromachines* **12**(3), 281 (2021).
17. Y. Hirakawa, T. Yoshihara, M. Kamiya, I. Mimura, D. Fujikura, T. Masuda, R. Kikuchi, I. Takahashi, Y. Urano, S. Tobita, and M. Nangaku, "Quantitating intracellular oxygen tension in vivo by phosphorescence lifetime measurement," *Sci. Rep.* **5**(1), 17838 (2015).
18. R. Sen, L. M. Hirvonen, A. Zhdanov, P. Svihra, S. Andersson-Engels, A. Nomerotski, and D. Papkovsky, "New luminescence lifetime macro-imager based on a Tpx3Cam optical camera," *Biomed. Opt. Express* **11**(1), 77–88 (2020).
19. M. Mosshammer, V. V. Scholz, G. Holst, M. Kuhl, and K. Koren, "Luminescence Lifetime Imaging of O<sub>2</sub> with a Frequency-Domain-Based Camera System," *J. Vis. Exp.* **154** (2019).
20. S. C. Leshner-Perez, G. A. Kim, C. H. Kuo, B. M. Leung, S. Mong, T. Kojima, C. Moraes, M. D. Thouless, G. D. Luker, and S. Takayama, "Dispersible oxygen microsensors map oxygen gradients in three-dimensional cell cultures," *Biomater Sci* **5**(10), 2106–2113 (2017).
21. A. C. Mitchell, J. E. Wall, J. G. Murray, and C. G. Morgan, "Direct modulation of the effective sensitivity of a CCD detector: a new approach to time-resolved fluorescence imaging," *J Microsc* **206**(3), 225–232 (2002).
22. A. C. Mitchell, J. E. Wall, J. G. Murray, and C. G. Morgan, "Measurement of nanosecond time-resolved fluorescence with a directly gated interline CCD camera," *J Microsc* **206**(3), 233–238 (2002).
23. L. M. Hirvonen, F. Festy, and K. Suhling, "Wide-field time-correlated single-photon counting (TCSPC) lifetime microscopy with microsecond time resolution," *Opt. Lett.* **39**(19), 5602–5605 (2014).

24. L. M. Hirvonen, Z. Petrášek, A. Beeby, and K. Suhling, "Sub- $\mu$ s time resolution in wide-field time-correlated single photon counting microscopy obtained from the photon event phosphor decay," *New J. Phys.* **17**(2), 023032 (2015).
25. B. Xiong and Q. Fang, "Luminescence lifetime imaging using a cellphone camera with an electronic rolling shutter," *Opt. Lett.* **45**(1), 81–84 (2020).
26. E. J. Gualda, T. Vale, P. Almada, J. A. Feijo, G. G. Martins, and N. Moreno, "OpenSpinMicroscopy: an open-source integrated microscopy platform," *Nat. Methods* **10**(7), 599–600 (2013).
27. F. Pampaloni, N. Ansari, and E. H. Stelzer, "High-resolution deep imaging of live cellular spheroids with light-sheet-based fluorescence microscopy," *Cell Tissue Res* **352**(1), 161–177 (2013).
28. C. Greb, "Infinity Optical Systems: From infinity optics to the infinity port," *Opt. Photonik* **11**(1), 34–37 (2016).
29. S. Grenoble, M. Gouterman, G. Khalil, J. Callis, and L. Dalton, "Pressure-sensitive paint (PSP): concentration quenching of platinum and magnesium porphyrin dyes in polymeric films," *J. Lumin.* **113**(1-2), 33–44 (2005).
30. K. R. Rivera, V. A. Pozdin, A. T. Young, P. D. Erb, N. A. Wisniewski, S. T. Magness, and M. Daniele, "Integrated phosphorescence-based photonic biosensor (iPOB) for monitoring oxygen levels in 3D cell culture systems," *Biosens. Bioelectron.* **123**, 131–140 (2019).
31. K. Koren, M. Mosshammer, V. V. Scholz, S. M. Borisov, G. Holst, and M. Kuhl, "Luminescence Lifetime Imaging of Chemical Sensors-A Comparison between Time-Domain and Frequency-Domain Based Camera Systems," *Anal. Chem.* **91**(5), 3233–3238 (2019).
32. G. T. Vladislavljjevic, H. Shahmohamadi, D. B. Das, E. E. Ekanem, Z. Tauanov, and L. Sharma, "Glass capillary microfluidics for production of monodispersed poly (DL-lactic acid) and polycaprolactone microparticles: experiments and numerical simulations," *J Colloid Interface Sci* **418**, 163–170 (2014).
33. J. C. Ribierre, A. Ruseckas, P. E. Shaw, H. S. Barcena, P. L. Burn, and I. D. W. Samuel, "Thickness Dependence of the Fluorescence Lifetime in Films of Bisfluorene-Cored Dendrimers," *J. Phys. Chem. C* **112**(51), 20463–20468 (2008).
34. A. Colom, R. Galgoczy, I. Almendros, A. Xaubet, R. Farré, and J. Alcaraz, "Oxygen diffusion and consumption in extracellular matrix gels: Implications for designing three-dimensional cultures," *J. Biomed. Mater. Res.* **102**(8), 2776–2784 (2014).
35. M. K. Lee, M. H. Rich, K. Baek, J. Lee, and H. Kong, "Bioinspired tuning of hydrogel permeability-rigidity dependency for 3D cell culture," *Sci. Rep.* **5**(1), 8948 (2015).
36. L. Figueiredo, R. Pace, C. D'Arros, G. Rethore, J. Guicheux, C. Le Visage, and P. Weiss, "Assessing glucose and oxygen diffusion in hydrogels for the rational design of 3D stem cell scaffolds in regenerative medicine," *J Tissue Eng Regen Med* **12**(5), 1238–1246 (2018).
37. N. A. Hosny, D. A. Lee, and M. M. Knight, "Single photon counting fluorescence lifetime detection of pericellular oxygen concentrations," *J. Biomed. Opt.* **17**(1), 016007 (2012).
38. K. Funamoto, I. K. Zervantonakis, Y. Liu, C. J. Ochs, C. Kim, and R. D. Kamm, "A novel microfluidic platform for high-resolution imaging of a three-dimensional cell culture under a controlled hypoxic environment," *Lab Chip* **12**(22), 4855–4863 (2012).
39. C. Schmitz, I. Pepelanova, C. Ude, and A. Lavrentieva, "Studies on oxygen availability and the creation of natural and artificial oxygen gradients in gelatin-methacryloyl hydrogel 3D cell culture," *J Tissue Eng Regen Med* **16**(11), 977–986 (2022).